Chirped pulse control over the melting of superconductors

Maria Recasens [1,*] Valentin Kasper,[1,†] Maciej Lewenstein [1,2] and Allan S. Johnson [3,‡]
[1]*ICFO - Institut de Ciencies Fotoniques, The Barcelona Institute of Science and Technology, Avenida Carl Friedrich Gauss 3, 08860 Castelldefels (Barcelona), Spain*
[2]*ICREA, Passeig de Lluis Companys 23, 08010 Barcelona, Spain*
[3]*IMDEA Nanoscience, Calle Faraday 9, 28023 Madrid, Spain*

(Received 2 April 2024; revised 9 January 2025; accepted 10 January 2025; published 20 February 2025)

Strong field terahertz pulses are increasingly used to excite and control quantum materials at the ultrafast timescale. They have found widespread application by enabling direct addressing of the superconducting gap or Josephson resonances and are essential in Higgs spectroscopy. Large non-linear optical signals can be induced by the strong coupling of the THz and superconducting degrees of freedom. However, far less attention has been paid to the strong bidirectional coupling between field and material this implies. Here, we use the framework of the time-dependent Ginzburg-Landau equations to study the full field and material evolution of a superconductor driven by strong field terahertz pulses. We find that at high field strengths, the backreaction of the superconductor induces large changes to the driving pulse, which in turn leads to a runaway melting of the superconducting condensate. This results in a surprisingly large sensitivity to the initial driving pulse chirp, enabling these purely dynamical changes to produce order of magnitude differences in the level of melting. We also find large-scale spectral shifting of the driving pulse to occur in just a few hundred nanometers of propagation through a superconductor. We attribute these effects to an inverse plasma redshift, in which the driving field breaks Cooper pairs and decreases the free-electron mobility, analogous to reducing the density of a plasma.

DOI: 10.1103/PhysRevB.111.064513

I. INTRODUCTION

Terahertz (THz) pulses have recently emerged as a powerful tool for exciting and controlling quantum materials. The low photon energies allow the THz radiation to couple the collective excitations efficiently in various systems. Furthermore, with the advent of high-field pulses with peak electric field strength of hundreds of kilovolts to megavolts per centimeter, it has become possible to drive quantum materials far out of equilibrium [1]. THz driving has been particularly successfully applied to superconductors with various low-energy collective modes. Examples include the use of THz driving to observe hidden stripe phases, parametrically amplify superconducting fluctuations, and coherently drive Higgs modes, leading to new forms of nonlinear spectroscopy, emergent phases, and control of superconductivity [2–4].

In many of these cases, it has been noted that the nonlinear response of the superconductor to the THz radiation is exceptionally large, with cross sections far greater than can be found in conventional materials [5,6]. This is true both when the THz is resonant to particular collective modes, but also works off resonance when the primary coupling is directly to the superconducting condensate [7,8]. Especially, in the latter case, the light field can drive large time-dependent supercurrents. Numerous studies and models have been made to explain these large nonlinear effects with focus upon the accurate treatment of the superconducting response [4,7,9]. However, at high fields it can be important to model the entire system of light and superconductor [8,10], i.e., the back reaction of the superconductor on the THz field. This back reaction can drastically modify the response of the system, and the ability to drive and control superconductors with light selectively [7]. As larger field strength THz pulses become available [11], this back reaction can be expected to be even more significant.

Here we present work modeling the impact of the superconducting back reaction on an intense THz driving field and how this strongly modifies the overall system dynamics. We directly model and solve a one-dimensional system to study the response of a superconducting condensate and the propagation of the THz driving laser field. Particularly, we treat the superconducting response via the phenomenological time-dependent Ginzburg Landau (TDGL) equations [8] and the field propagation by the full Maxwell equations. We focus on the effect of the initial chirp of the pulse in the interaction [12]. The chirp of the pulse determines how its frequency changes over time. In a linearly chirped pulse, for instance, the frequency increases (positive chirp) or decreases (negative chirp) continuously throughout the duration of the pulse. Our results demonstrate a large dependence of the system on the initial pulse chirp at high THz field strengths, with realistic

*Contact author: maria.recasens@icfo.eu
†Contact author: valentin.kasper@icfo.eu
‡Contact author: allan.johnson@imdea.org

chirp variations leading to differences in the melting of the superconducting condensate of up to one order of magnitude. This dependence is attributed to a spectral shift in the driving pulse occurring within a range of a few hundred nanometers. We associate this spectral shift with the breaking of Cooper pairs caused by the pulse, giving rise to an inverse plasma redshift effect [13]. The substantial nonlinear response observed in the superconductor has the potential to improve control and diagnostics of superconductivity.

II. MODEL

A wide variety of models have been used previously to describe the dynamics of superconductors out of equilibrium. These include microscopic models like the time-dependent Gutzwiller variational approach or time-dependent dynamical mean field theory; see [14] for a review. On the other hand phenomenological models, such as the two-temperature model or the Rothwarf-Taylor model [15], can return qualitative understanding about the melting process but generally do not directly treat the coupling between laser pulses and superconductors.

For our simulations, we use the time-dependent Ginzburg Landau theory coupled to the Maxwell equations. The TDGL equation describes the dynamics of the superconductor order parameter ψ and the Maxwell equations the propagation of the EM field. The TDGL equation was derived by Schmidt [16], and later Gor'kov and Eliashberg showed that it could also be derived from the BCS theory in the case of gapless superconductors [17]. The order parameter ψ can be directly related to the Cooper pair density n_c via $n_c = |\psi|^2$ through BSC theory. Critically, TDGL makes concrete and quantitative predictions for a wide variety of dynamical behaviors, such as the dynamics of vortices in type II superconductors [18–22] or of fluctuations in the conductivity above T_c [23]. TDGL has previously been applied to studying THz driving of superconductors, where it was found that TDGL could semiquantitatively describe the giant Kerr response in superconductors [8,10]. We briefly note that an alternative approach to treat the complete field + superconductor system would be models based on the Boguliobov–de Gennes Hamiltonian [24–26].

The TDGL equation [27] is

$$\frac{\hbar^2}{2m^* D}\frac{\partial \psi}{\partial t} = \frac{\partial f}{\partial \psi^*}, \tag{1}$$

where D is the diffusion coefficient, m^* is the effective mass of the Cooper pair, and f is the free energy, where we already implicitly assume the temporal gauge $\phi = 0$. In the Ginzburg-Landau equation for superconductivity, the free energy is given by

$$f = f_n + a|\psi|^2 + \frac{b}{2}|\psi|^4 + \frac{1}{2m^*}|(-i\hbar\nabla - e^*\mathbf{A})\psi|^2, \tag{2}$$

where $a = a_0(T - T_c)$, a_0 and b are constants of the material, e^* and m^* are the effective charge and mass of the Cooper pairs, and $\boldsymbol{A}$ is the vector potential that represents the external light field. The parameters a_0 and b can be determined through their relationships to the experimentally measurable London penetration depth λ and coherence length ξ, which are defined as

$$\xi(T) = \sqrt{\hbar^2/(2m^*|a(T)|)}, \tag{3a}$$

$$\lambda(T) = \sqrt{m^*/(4\mu_0 e^2|\psi_0|^2)}, \tag{3b}$$

$$|\psi_0|^2 = -a_0/b, \tag{3c}$$

$$\tau = \xi^2/D \tag{3d}$$

where $|\psi_0|^2$ is the solution of the TDGL equation in the case of no spatial dependence and no electromagnetic field applied. The Ginzburg-Landau parameter, $\kappa = \lambda/\xi$, can also be obtained through these quantities.

By inserting the free energy of Eq. (2) in Eq. (1), we obtain

$$\frac{\hbar^2}{2m^* D}\frac{\partial \psi}{\partial t} = \frac{1}{2m^*}(-i\hbar\partial_j - 2eA_j)^2\psi - (a + b|\psi|^2)\psi. \tag{4}$$

Further, we rewrite the TDGL using the abbreviation introduced in Eq. (3), leading to

$$\tau\partial_t\psi = \xi^2\left(-i\partial_j - \frac{2e}{\hbar}A_j\right)^2\psi + \left(\frac{T_c - T}{T_c} - \frac{|\psi|^2}{|\psi_0|^2}\right)\psi. \tag{5}$$

To describe the superconductor interaction with the EM pulse, it is also necessary to include in the model the supercurrent equation, i.e., the dissipationless current,

$$J_s = \frac{e^*}{m^*}\,\mathrm{Re}[\psi^*(-i\hbar\nabla - e^*\mathbf{A})\psi], \tag{6}$$

where ψ^* is the complex conjugate of ψ and Re denotes the real part [28].

Furthermore, to fully describe the coupled system, we also need to include the response of the electrons outside of the condensate state. Here, we use the Drude model to consider the remaining electrons of the superconductor not bound into Cooper pairs. The evolution of the electric field is, as a result, described by

$$\partial_t E_x(y,t) = \epsilon_0^{-1}\partial_y H_z(y,t) + \epsilon_0^{-1}[J_d(t) + J_s(y,t)], \tag{7a}$$

$$\partial_t H_z(y,t) = \mu_0^{-1}\partial_y E_x(y,t), \tag{7b}$$

where ϵ_0 is the permittivity of free space and J_d is the Drude current, whose dynamics are described by

$$\partial_t J_d(t) = -\gamma J_d(t) + \omega_p^2\epsilon_0 E_x(y,t), \tag{8}$$

where γ is a damping factor and ω_p the plasma frequency. Thus, the entire system of equations that we solve to describe the material response and field evolution is given by Eqs. (5)–(8). The TDGL theory is valid within the limitation that the superconducting order parameter must evolve slowly relative to microscopic timescales, allowing the quasiparticle system to maintain local equilibrium. This condition requires the characteristic frequency of the fluctuations of the order parameter to be slower than the inelastic scattering rate of the quasiparticles [28,29]. In our calculations, we ensure this constraint by simulating a gapless superconductor, where paramagnetic impurities and strong electron-phonon scattering enhance the inelastic scattering rate, promoting rapid local equilibration of quasiparticles. Furthermore, we apply the TDGL theory near the critical temperature, where the

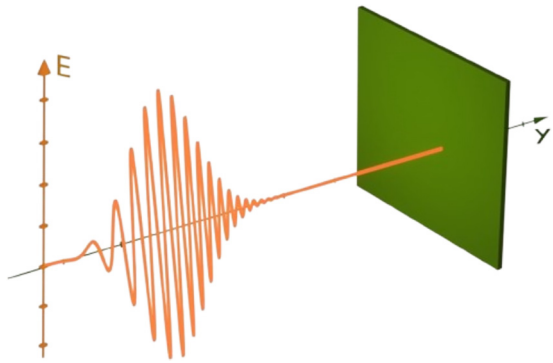

FIG. 1. Simulation setup. We consider a thin, infinite two-dimensional superconducting plate (green) and a chirped probing pulse (orange).

order parameter has a long relaxation time, ensuring the slow evolution criterion. These considerations collectively ensure that our application of the TDGL theory remains within its domain of validity.

Due to their frequency range, THz pulses couple most effectively to the superconducting condensate itself, rather than to the normal phase, thus we neglect other indirect heating channels which can be treated using TDGL extensions and are more relevant at optical frequencies [30].

A. Geometry and setup

To investigate the back reaction of a superconductor on a THz field, we simulate the case of a high-field THz pulse incident on bulk material. Specifically, we focus on the effect of the initial chirp of the pulse, as introducing a frequency chirp modifies the pulse without affecting the total energy of the pulse. In particular, we model the scenario of a THz pulse hitting a superconducting thin film as illustrated in Fig. 1, allowing us to describe the system in one spatial dimension. For the explained geometry of the simulation, the order parameter ψ can be treated as dependent only on y.

B. Pulse and material

The dynamics of a superconductor driven by a THz pulse will depend on the parameters describing the geometry, the incident pulse, and the properties of the material. Concerning the incoming pulse, we mainly focus on the pulse chirp. Tuning the chirp does not change the total input energy, which gives a unique look at the dynamic response of the system.

Regarding the driving THz field, we start from a simple Gaussian pulse with an electric field given by

$$E(t) = E_0 e^{-(t-t_0)^2/t_g^2} \sin\left[\omega_0(t-t_0)\right], \tag{9}$$

where E_0 is the electric field strength, t_g determines the width of the envelope in the time domain, ω_0 is the angular photon frequency, and t_0 is the center of the pulse in the time domain.

We include the chirp by multiplying the Fourier transform of the pulse given in Eq. (9) with

$$e^{-i[a(\omega-\omega_0)+b(\omega-\omega_0)^2+c(\omega-\omega_0)^3+\cdots]} \tag{10}$$

and then Fourier transforming back to the time domain, where a quantifies the scalar phase shift, b the linear chirp, and ω are the angular frequencies that compose the pulse spectra. This pure phase addition stretches the pulse in the time domain but does not change the total energy or the spectral content. Instead, it modifies the arrival time of the different spectral components. To obtain a chirp of order $n-1$, we add a term proportional to $(2\pi f - \omega_0)^n$ in the exponent of Eq. (10).

Concerning the initial pulse, we explore a range of field strengths spanning one order of magnitude, from $0.6\,\mathrm{MVcm}^{-1}$ to $6\,\mathrm{MVcm}^{-1}$ for the unchirped pulses. These fields are high, but technically feasible [11]. Further, we note that using thinner samples enables the replication of the results at lower field strengths. We consider photon frequencies ranging from the THz to the midinfrared domain with $t_g = 132\,\mathrm{fs}$ and $\omega_0 = 4.9\,\mathrm{THz}$. As for the frequency chirp, we introduce a linear chirp, keeping the parameters $a = c = 0$.

Motivated by experiment, we consider a 230 nm thick film of lead, with a critical temperature of T_c of 7.2 K; see [31]. The material choice determines the TDGL parameters. For a BCS superconductors superconductor, m^* and e^* take straightforward values related to the Cooper-pair structure, $m^* = 2m_e$ and $e^* = 2e$ [17,32]. For lead, the remaining parameters take the values $\xi = 82\,\mathrm{nm}$, $\kappa = 0.48$ [31], $w_p = 0.307\,\mathrm{fs}^{-1}$, and $\gamma = 11.188\,\mathrm{fs}^{-1}$. The simulations are initialized with the system in equilibrium at $T = 6\,\mathrm{K}$.

III. RESULTS

We calculate the propagation of the pulse and the dynamics of the material by numerically integrating the system of equations (5)–(8). At the boundaries of the material, we enforce $J_s \cdot n = 0$, and generate the propagating pulse using a source far away from the material. To avoid reflections of the EM pulse at the boundaries of the simulation, we added perfectly matched layers far away from the source and the material. Finally, we discretize space using finite differences and solve the time evolution with a fourth-order Runge-Kutta solver. In the following subsections, we analyze our simulation results, focusing on the influence of the chirp. We analyze the effect of the sign of the chirp, the response of the superconducting order parameter concerning the chirp, and the response of the electromagnetic field.

A. Positive chirp and negative chirp

We simulate the interaction between the superconductor and the pulse for two different pulses, one with positive and one with negative chirp. Figure 2(a) illustrates the electric field of pulses with chirps of 20×10^3, 0, and $-20 \times 10^3\,\mathrm{fs}^2$. The high-frequency components arrive first for positive chirps, while for negative chirps we observe the opposite.

In Fig. 2, we study the spatial and temporal results of the described simulations. Specifically, Figs. 2(b) and 2(d) show the results for the negative linear chirp, whereas Figs. 2(c) and 2(e) depict the results for the positive linear chirp. By comparing the left and right columns, we note that the two scenarios show significant qualitative differences in the evolution of the superconductor. Specifically, we observe a more significant suppression of the order parameter for negative chirps, and

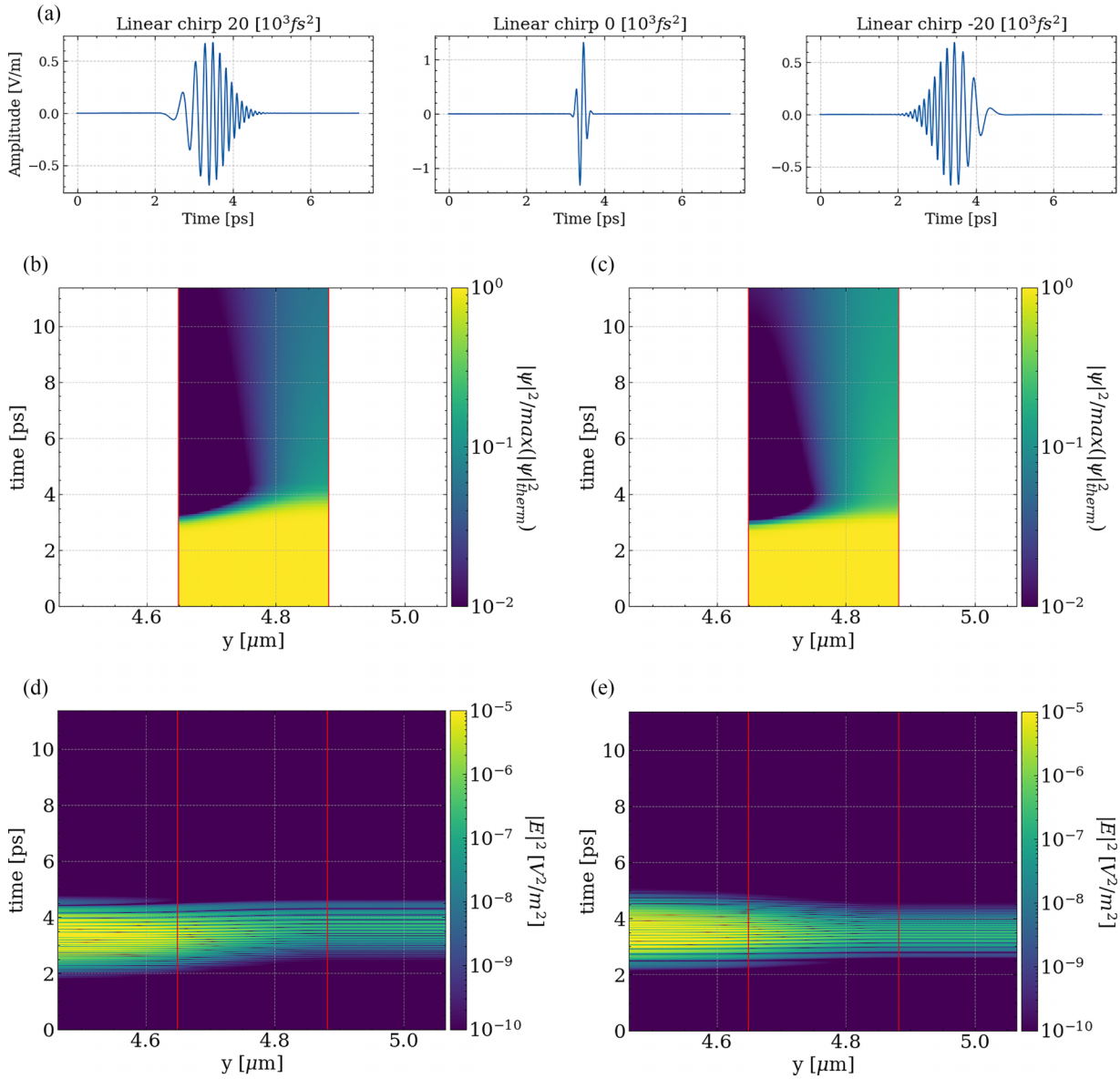

FIG. 2. Pulse sequence and spatiotemporal distribution of order parameter. Interaction between the superconductor and the electromagnetic pulse for a peak field strength of 6 MVcm^{-1} for the unchirped pulse. The red lines represent the boundaries of the superconductor. In panel (a) we show the electric field of EM pulses with different linear frequency chirps. Further, in panels (b) and (c) we show the order parameter as a function of time and space normalized by the maximum value of the initial thermal state, $|\psi|^2/|\psi_{\max}|^2$, where $|\psi_{\max}|^2 = 1.52\,\mathrm{nm}^{-3}$. In subfigures (d) and (e) we show the time and space evolution of the electric field amplitude squared, E^2 in $\mathrm{V}^2/\mathrm{m}^2$. The explicit value of the chirp is $b = -20 \times 10^3\ \mathrm{fs}^2$ in (b) and (d), and $b = 20 \times 10^3\ \mathrm{fs}^2$ in (c) and (e).

the suppression occurs at earlier times for the positive chirp case. In addition, Figs. 2(d) and 2(e) show the evolution of the corresponding EM pulse inside the superconductor. For the pulse with positive chirp [see Fig. 2(e)] we observe that low and high frequencies are similarly suppressed inside the superconductor, whereas for the negative chirp pulse [see Fig. 2(d)], high frequencies are more suppressed than lower frequencies. These differences indicate tuning the response of the material by the sign of the chirp.

B. Suppression of superconductivity using the chirp

To gain more insight into the chirp dependence of the dynamics, we systematically vary the chirp and quantify the extinction of the order parameter. This is done by evaluating the integral

$$\Psi = \frac{1}{C}\int_y |\psi(y)|^2\, dy, \tag{11}$$

where C is a normalization factor defined as $C = \int_y |\psi(y)_{\mathrm{therm}}|^2\, dx$. Here $\psi(y)_{\mathrm{therm}}$ is the spatial distribution of the order parameter in the superconductor before the laser excitation, for the specific geometry of the simulation. We record the value of Ψ at the end of the simulation, specifically at 12 ps.

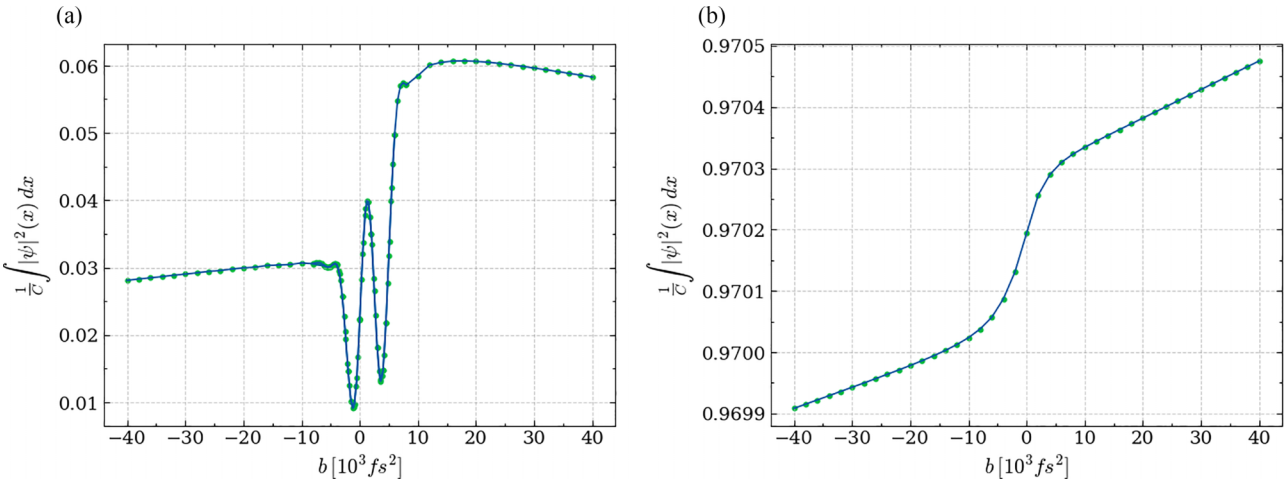

FIG. 3. Tuning order parameter with linear chirp. The integral in space of the order parameter, $\Psi = \frac{1}{C}\int_y |\psi(y)|^2\,dy$, after the pulse has passed the superconductor, at $t = 12$ ps, for two different initial field strengths. The value of the integral is normalized by $C = \int_y |\psi(y)_{\text{therm}}|^2\,dy$. Where $\psi(y)_{\text{therm}}$ is the spatial distribution of the order parameter in the superconductor before the laser excitation, for the specific geometry of the simulation. In panels (a) and (b), we use peak field strengths of 6 and 0.6 MVcm^{-1} respectively for $b = 0$.

The results of this study are given in Fig. 3 where we show $\Psi(y)$ as a function of the linear chirp of the source pulse for two different field strengths one order of magnitude apart.

In both plots, we can clearly differentiate three distinct regions. One for large negative chirps, another for low chirps, and a third for large positive chirps. In the large chirp regions, we can see that negatively chirped pulses suppress the order parameter more than positively chirped pulses. Thus, negative chirped pulses more effectively destroy superconductivity than positive chirped ones. As we discuss in the following section, this marked difference arises from the dependence of the back reaction of the superconductor on the sign of the chirp. As different pulses with the same magnitude of chirp but opposite sign have identical pulse durations, we can uniquely attribute this effect as dynamically resulting from the time-varying frequency. This result holds for an extensive range of field strengths, although the magnitude of the effect changes significantly. In addition to this effect, around zero chirp, there are clear oscillations in $\Psi(y)$ with chirp, along with exceptionally high suppression of the amplitude, in the high field case.

C. Optical back reaction

To understand the origin of these changes in suppression, we first examine the transmission of the pulse as a function of chirp, as shown in Fig. 4, given by

$$T = \frac{\int_y |E_{\text{transmitted}}(y)|^2\,dy}{\int_y |E_{\text{source}}(y)|^2\,dy}. \tag{12}$$

We focus on the high field case where the effects are more dramatic. We immediately note the changes observed in Fig. 3 do not directly map to changes in transmission because the asymmetry between positive and negative chirps is small. However, the absorption increases dramatically for small chirp values at the highest pulse intensity. This behavior does not follow a simple power law of intensity. It thus suggests that for low-chirp, high-intensity pulses, additional nonlinear melting processes of the condensate become significant. We have verified this assertion by performing additional scans under zero chirp conditions in which we keep the total energy in the pulse constant but change t_g, leading to a decrease in peak field, which indeed confirms a nonlinear melting process occurs at high field strengths; see Supplemental Material Fig. S1 [33]. Moreover, oscillations also appear in this low-chirp regime, although their physical origin remains unclear to us and requires further investigation. Given thus the different nature of the effects in the low-chirp regime vs large-chirp regime, we focus our subsequent analysis on the large-chirp regime where we have established a clear physical framework for the observed phenomena.

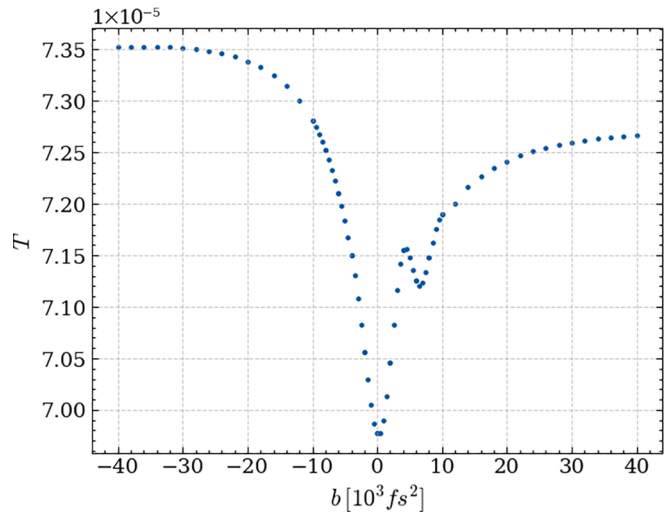

FIG. 4. Transmission coefficient: For different chirps, we depict the total transmitted energy after the material normalized by the total energy of the source pulse for a peak field strength of 6 MVcm^{-1} at $b = 0$. We observe a clear minimal transmission coefficient close to zero chirp, and observe asymmetric tuning of the transmission for positive and negative chirps.

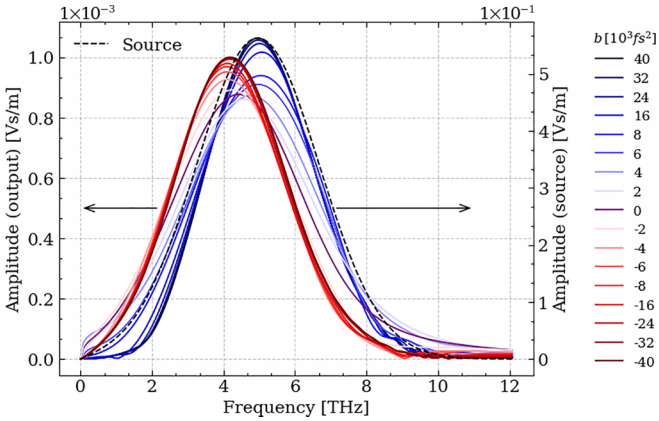

FIG. 5. Spectrum of the laser pulse after interaction. Spectra of the pulse after the material for a field strength of 6 MVcm^{-1}. Red solid lines correspond to the spectra of the pulses with negative chirps, purple solid lines to the spectra of the Gaussian pulse without chirp, and blue solid lines to the spectra of the positive chirped pulses. The dashed black line corresponds to the input spectra of the source, which is the same for all chirps.

As changes in total absorption cannot explain the strongly asymmetric melting process, we next examine the back reaction of the superconductor on the spectrum of the pulse. Figure 5 displays the spectra of the source pulse and the output pulse spectrum for a range of chirps. Solid lines correspond to the spectra of pulses after going through the material, and the dashed black line is the spectra of the source pulses. We see a clear spectra shift towards lower frequencies for large negative chirps. On the other hand, for large positive chirps, we did not observe a shift or asymmetric narrowing of the spectra. This offers a partial explanation for the behavior of the superconductor: low frequencies couple more strongly to the condensate [8] and lead to a nonthermal suppression of the superconducting condensate, and hence this giant redshift enhances the nonthermal melting process. A redshift of this type has previously been predicted for THz-driven superconductors, but only under the zero-chirp condition, where we see a significantly smaller redshift [10]. As the magnitude of the chirp further increases, we see the effect begin to saturate and gradually decrease for the high-field case. This is consistent with the decrease in peak intensity leading to a gradual decrease in the amplitude of the time-dependent refractive index change.

D. Asymmetric spectral broadening and melting

Previous work [10] related the melting of superconductivity to a giant asymmetric third-order nonlinear optical response. Here, we offer an intuitive explanation of this effect and how this leads to a strong chirp sensitivity of the melting process. A driven material with a refractive index that varies over time modulates the phase of the driving field, leading to new frequencies, i.e., self-phase modulation [34]. Typically, the refractive index follows a simple rule $n(t) = n_0 + 3\chi^{(3)}I(t)/(4n_0^2\epsilon_0 c)$, where n_0 is the static refractive index, $\chi^{(3)}$ is the third-order nonlinear susceptibility and $I(t)$ is the intensity of the driving pulse. Because $n(t)$ then follows the temporal behavior of $I(t)$, there is a region where $n(t)$ increases, then decreases. For a positive $\chi^{(3)}$, which describes most materials, increased intensities lead to an increase in refractive index and a redshift, while decreased intensities lead to a blueshift [34].

In a superconductor, however, the leading contributions to $\chi^{(3)}$ come from the melting of the superconducting condensate [8]. In this case, $n(t)$ does not follow $I(t)$ as the pulse can only melt the superconducting condensate, and the evolution of $n(t)$ is monotonic. This is conceptually very close to the idea of the plasma-blue shift: in a gas ultrafast laser ionization generates free carriers, leading to the formation of a plasma and a blueshift in the driving laser frequency because of the associated time-dependent decrease in the refractive index [13,35]. However, in a superconductor, the inverse effect is at play: by breaking Cooper pairs (effectively melting a high-mobility plasma), we dynamically reduce the effective free-carrier response, leading to a redshift. Robson *et al.* [8], derived an approximate expression for $\chi^{(3)}$ in superconductors:

$$\chi^{(3)} = -\frac{128k_b^2(T-T_c)^2e^4}{\epsilon_0\beta\omega_0^6\pi^2\hbar^2m_e^2}, \tag{13}$$

where k_b is the Boltzmann constant. As can be seen, low frequencies (small ω_0) dramatically increase the Kerr-like response of the superconductor. So, the redshift in the driving pulse, in turn, more effectively melting the superconducting condensate and dynamically reinforces the melting process in a positive feedback loop, as alluded to above. This inverse plasma redshift intuitively explains the giant redshift [10] and why the redshifted pulse is linked to more substantial melting.

Next, we consider the role of the chirp explicitly. That the sign of chirp dramatically affects the degree of broadening induced by nonlinear processes has long been known for conventional self-phase modulation [36], with the exact behavior depending on whether the newly generated frequencies are additive or out of phase with existing spectral components of the pulse. However, in the case of a melting the superconductor condensate, there is an additional history effect, as the magnitude of $\chi^{(3)}$ is directly related to the number of Cooper pairs that remain in the sample, as represented by the $(T-T_c)^2$ factor in Eq. (13). A positively chirped pulse thus redshifts the low-frequency components effectively, leading to very strong superconducting suppression in the leading edge of the pulse but comparatively little redshifting in the trailing edge. As such, only the leading edge effectively melts the superconducting condensate, as can be seen by examining Fig. 2(c), leads to the most substantial absorption at these frequencies. In contrast, the trailing high-frequency edge undergoes only a minor redshift.

In contrast, for a negative chirped pulse, the redshift is strongest for high-frequency components, and the overall melting process is more evenly distributed throughout the duration of the pulse, as seen in Fig. 2(b). This leads to a more even shift to low frequencies across the whole bandwidth and allows the total spectral bandwidth to contribute to the suppression of the superconductivity. Thus, this history effect explains why both the redshift of negatively chirped pulses and the narrowing of positively chirped pulses saturate so

effectively in Fig. 5, and why the effects depend intimately on the particular nature of the melting of the superconducting condensate.

IV. CONCLUSION

With increasingly high-field terahertz pulses being used to manipulate superconductors, the back reaction of the superconductor upon the driving pulse will become more and more significant. Here, we have presented a study of the entire field and material evolution of a BCS-type superconductor driven by high-field strength THz pulses through a clear and transparent approach based on the TDGL theory. We find the dynamics of the superconductor to be strongly dependent on the initial chirp of the driving pulse, leading to variations up to one order of magnitude of the melting of the superconducting condensate and large-scale spectral shifting of the driving pulse within a few hundred nanometers of propagation through a superconductor. We attribute these dynamics to an inverse plasma redshift response of the condensate. Similarly to the plasma-blueshift phenomena known in plasma physics, here the destruction of Cooper pairs caused by the driving field effectively decreases the free-carrier density/mobility, causing a time-dependent change of the refractive index, which redshifts the driving field, leading to stronger nonthermal suppression of the condensate. In the limit of strong melting, this shift depends upon the history of the pulse, so the input chirp can modulate the overall degree of melting significantly.

This history effect and giant redshift are rather unique features of superconductors. Thus, the uncovered high dependence of the state of the superconductor on purely dynamical variables, such as the chirp, indicates that pulse shaping could be an interesting tool for the control and diagnosis of superconductivity. It also suggests that superconductors could form an interesting class of nonlinear optic materials in the THz regime. Our simulations show that macroscopic models of the superconductor-light interaction can reveal unexpected effects in the dynamics of such systems and may need to be explicitly treated to understand experiments performed at high field strengths.

ACKNOWLEDGMENTS

This work was funded by the Spanish AIE (Projects No. PID2022-137817NA-I00 and No. EUR2022-134052). ICFO group acknowledges support from ERC AdG NOQIA; MCIN/AEI [PGC2018-0910.13039/501100011033, CEX2019-000910-S/10.13039/501100011033, Plan National FIDEUA PID2019-106901GB-I00, Plan National STAMEENA PID2022-139099NB-I00 project funded by MCIN/AEI/10.13039/501100011033 and by the "European Union NextGenerationEU/PRTR" (PRTR-C17.I1), FPI]; QUANTERA MAQS PCI2019-111828-2; QUANTERA DYNAMITE PCI2022-132919 (QuantERA II Programme co-funded by European Union's Horizon 2020 program under Grant Agreement No 101017733); Ministry for Digital Transformation and of Civil Service of the Spanish Government through the QUANTUM ENIA project call - Quantum Spain project and through the European Union through the Recovery, Transformation and Resilience Plan - NextGenerationEU within the framework of the Digital Spain 2026 Agenda; Fundació Cellex; Fundació Mir-Puig; Generalitat de Catalunya (European Social Fund FEDER and CERCA program, AGAUR Grant No. 2021 SGR 01452, QuantumCAT U16-011424, cofunded by ERDF Operational Program of Catalonia 2014–2020); Barcelona Supercomputing Center MareNostrum (FI-2023-1-0013); EU Quantum Flagship (PASQuanS2.1, 101113690, funded by the European Union; EU Horizon 2020 FET-OPEN OPTOlogic (Grant No 899794); EU Horizon Europe Program (Grant Agreement No. 101080086–NeQST). Results incorporated in this standard have received funding from the European Innovation Council and SMEs Executive Agency under the European Union's Horizon Europe programme); ICFO Internal "QuantumGaudi" project; European Union's Horizon 2020 program under the Marie Sklodowska-Curie Grant Agreement No 847648; "La Caixa" Junior Leaders fellowships, La Caixa Foundation (ID 100010434): CF/BQ/PR23/11980043. M.R. acknowledges the support of a Joan Oró Fellowship (2024FI-200017). A.S.J. acknowledges the support of the Ramón y Cajal Program (Grant No. RYC2021-032392-I). IMDEA Nanociencia acknowledges support from the "Severo Ochoa" Programme for Centers of Excellence in R&D (MICIN, CEX2020-001039-S).

Views and opinions expressed are, however, those of the author(s) only and do not necessarily reflect those of the European Union, European Commission, European Climate, Infrastructure and Environment Executive Agency (CINEA), or any other granting authority. Neither the European Union nor any granting authority can be held responsible for them.

[1] C. Yang, J. Li, M. Fiebig, and S. Pal, Terahertz control of many-body dynamics in quantum materials, Nat. Rev. Mater. **8**, 518 (2023).

[2] A. Cavalleri, Photo-induced superconductivity, Contemp. Phys. **59**, 31 (2018).

[3] M. Budden, T. Gebert, M. Buzzi, G. Jotzu, E. Wang, T. Matsuyama, G. Meier, Y. Laplace, D. Pontiroli, M. Riccò *et al.*, Evidence for metastable photo-induced superconductivity in K3C60, Nat. Phys. **17**, 611 (2021).

[4] R. Shimano and N. Tsuji, Higgs mode in superconductors, Annu. Rev. Condens. Matter Phys. **11**, 103 (2020).

[5] R. Matsunaga, N. Tsuji, H. Fujita, A. Sugioka, K. Makise, Y. Uzawa, H. Terai, Z. Wang, H. Aoki, and R. Shimano, Light-induced collective pseudospin precession resonating with Higgs mode in a superconductor, Science **345**, 1145 (2014).

[6] H. Chu, M.-J. Kim, K. Katsumi, S. Kovalev, R. D. Dawson, L. Schwarz, N. Yoshikawa *et al.*, Phase-resolved Higgs response in superconducting cuprates, Nat. Commun. **11**, 1793 (2020).

[7] T. Cea, C. Castellani, and L. Benfatto, Nonlinear optical effects and third-harmonic generation in superconductors: Cooper pairs versus Higgs mode contribution, Phys. Rev. B **93**, 180507(R) (2016).

[8] C. W. Robson, K. A. Fraser, and F. Biancalana, Giant ultrafast Kerr effect in superconductors, Phys. Rev. B **95**, 214504 (2017).

[9] J. Demsar, Non-equilibrium phenomena in superconductors probed by femtosecond time-domain spectroscopy, J. Low Temp. Phys. **201**, 676 (2020).

[10] C. W. Robson and F. Biancalana, Giant asymmetric self-phase modulation in superconductor thin films, Mater. Res. Express **5**, 046001 (2018).

[11] C. Rader, Z. Zaccardi, S.-H. E. Ho, K. Harrell, P. Petersen, M. Nielson, H. Stephan, N. Green, D. Ludlow, M. Lutz, S. Smith, D. Michaelis, and J. Johnson, A new standard in high-field terahertz generation: the organic nonlinear optical crystal pnpa, ACS Photonics **9**, 3720 (2022).

[12] W. S. Warren, H. Rabitz, and M. Dahleh, Coherent control of quantum dynamics: the dream is alive, Science **259**, 1581 (1993).

[13] N. Bloembergen, The influence of electron plasma formation on superbroadening in light filaments, Opt. Commun. **8**, 285 (1973).

[14] C. Giannetti, M. Capone, D. Fausti, M. Fabrizio, F. Parmigiani, and D. Mihailovic, Ultrafast optical spectroscopy of strongly correlated materials and high-temperature superconductors: a non-equilibrium approach, Adv. Phys. **65**, 58 (2016).

[15] G. Coslovich, C. Giannetti, F. Cilento, S. Dal Conte, G. Ferrini, P. Galinetto, M. Greven, H. Eisaki, M. Raichle, R. Liang *et al.*, Evidence for a photoinduced nonthermal superconducting-to-normal-state phase transition in overdoped $Bi_2Sr_2Ca_{0.92}Y_{0.08}Cu_2O_{8+\delta}$, Phys. Rev. B **83**, 064519 (2011).

[16] A. Schmid, A time dependent Ginzburg-Landau equation and its application to the problem of resistivity in the mixed state, Phys. Kondens. Mater. **5**, 302 (1966).

[17] L. P. Gor'kov, Microscopic derivation of the Ginzburg–Landau equations in the theory of superconductivity, Zh. Eksp. Teor. Fiz. **36**, 1918 (1959) [Sov. Phys. JETP **9**, 1364 (1959)].

[18] A. T. Dorsey, Vortex motion and the Hall effect in type-II superconductors: A time-dependent Ginzburg-Landau theory approach, Phys. Rev. B **46**, 8376 (1992).

[19] M. Machida and H. Kaburaki, Direct simulation of the time-dependent Ginzburg-Landau equation for type-II superconducting thin film: Vortex dynamics and *V-I* characteristics, Phys. Rev. Lett. **71**, 3206 (1993).

[20] M. Ghinovker, B. Y. Shapiro, and I. Shapiro, Spontaneous magnetic-flux generation in superconducting ring, Europhys. Lett. **53**, 240 (2001).

[21] A. Kapra, V. Misko, D. Vodolazov, and F. Peeters, The guidance of vortex–antivortex pairs by in-plane magnetic dipoles in a superconducting finite-size film, Supercond. Sci. Technol. **24**, 024014 (2011).

[22] R. Hung, D. Berco, I. Y. Shapiro, B. Shapiro, and B. Rosenstein, Electrodynamics of type-II superconductor with periodic pinning array, Comput. Phys. Commun. **182**, 81 (2011).

[23] H. Schmidt, The onset of superconductivity in the time dependent Ginzburg-Landau theory, Z. Phys. A **216**, 336 (1968).

[24] C. Vaswani, J. H. Kang, M. Mootz, L. Luo, X. Yang, C. Sundahl, D. Cheng, C. Huang, R. H. J. Kim, Z. Liu, Y. G. Collantes, E. E. Hellstrom, I. E. Perakis, C. B. Eom, and J. Wang, Light quantum control of persisting Higgs modes in iron-based superconductors, Nat. Commun. **12**, 258 (2021).

[25] L. Luo, M. Mootz, J.-H. Kang, C. Huang, K. Eom, J. Lee, C. Vaswani, Y. Collantes, E. Hellstrom, I. E. Perakis *et al.*, Quantum coherence tomography of light-controlled superconductivity, Nat. Phys. **19**, 201 (2023).

[26] M. Mootz, J. Wang, and I. E. Perakis, Lightwave terahertz quantum manipulation of nonequilibrium superconductor phases and their collective modes, Phys. Rev. B **102**, 054517 (2020).

[27] W. Gropp, H. Kaper, G. Leaf, D. Levine, M. Palumbo, and V. Vinokur, Numerical simulation of vortex dynamics in type-II superconductors, J. Comput. Phys. **123**, 254 (1996).

[28] M. Tinkham, *Introduction to Superconductivity*, 2nd ed. (Dover, Mineola, NY, 2015)

[29] E. Abrahams and T. Tsuneto, Time variation of the Ginzburg-Landau order parameter, Phys. Rev. **152**, 416 (1966).

[30] V. R. Misko, S. Savel'ev, A. L. Rakhmanov, and F. Nori, Nonuniform self-organized dynamical states in superconductors with periodic pinning, Phys. Rev. Lett. **96**, 127004 (2006).

[31] R. Wesche, High temperature superconductors, in *Handbook of Electronic and Photonic Materials* (Springer, Cham, 2017)

[32] B. Cabrera and M. E. Peskin, Cooper-pair mass, Phys. Rev. B **39**, 6425 (1989).

[33] See Supplemental Material at http://link.aps.org/supplemental/10.1103/PhysRevB.111.064513 for additional data, derivations, and figures supporting the results.

[34] R. W. Boyd, *Nonlinear Optics* (Academic, New York, 2008).

[35] A. Giulietti and D. Giulietti, Self-phase modulation in various regimes of intense laser–plasma interactions, J. Plasma Phys. **81**, 495810608 (2015).

[36] M. Oberthaler and R. A. Höpfel, Special narrowing of ultrashort laser pulses by self-phase modulation in optical fibers, Appl. Phys. Lett. **63**, 1017 (1993).